

Extended Lyman- α emission around bright quasars *

L. Christensen^{1,2}, K. Jahnke^{2,3}, L. Wisotzki², and S. F. Sánchez⁴

¹ European Southern Observatory, Casilla 19001, Santiago 19, Chile, e-mail: lchrist@eso.org

² Astrophysikalisches Institut Potsdam, An der Sternwarte 16, 14482 Potsdam, Germany

³ Max Planck Institut für Astronomie, Königstuhl 17, 69117 Heidelberg, Germany

⁴ Centro Astronomico Hispano Alemán de Calar Alto, Calle Jesús Durbán Remón 2, 2 E-04004 Almería, Spain

Received ; accepted

ABSTRACT

Context. Quasars trace the most massive structures at high redshifts and their presence may influence the evolution of the massive host galaxies.

Aims. We study the extended Ly α emission line regions (EELRs) around seven bright, mostly radio-quiet quasars (QSOs) at $2.7 < z < 4.5$, and compare luminosities with EELRs around radio-loud QSOs reported in the literature.

Methods. Using integral field spectroscopy, we analyse the morphology and kinematics of the quiescent Ly α EELRs around the QSOs.

Results. We find evidence for the presence of EELRs around four radio-quiet and one radio-loud QSO. All EELRs appear asymmetric and the optically brightest QSOs also have the brightest Ly α nebulae. For the two brightest nebulae we find velocities between $\sim 600 \text{ km s}^{-1}$ at the QSO position to $\sim 200 \text{ km s}^{-1}$ at a distance of $3 - 4''$ from the QSO and surface flux densities up to $2 - 3 \times 10^{-16} \text{ erg cm}^{-2} \text{ s}^{-1} \text{ arcsec}^{-2}$. The five EELRs have total Ly α luminosities which correspond to $\sim 0.5\%$ of the luminosities from the QSOs broad Ly α emission lines. This fraction is an order of magnitude smaller than found for EELRs around radio-loud, steep spectrum QSOs reported in the literature. While the nebulae luminosities are correlated with the QSO Ly α luminosities, we find that nebulae luminosities are not correlated with the central QSO ionising fluxes.

Conclusions. The presence of gas in the EELRs can be interpreted based on two competing scenarios: either from quasar feedback mechanisms, or from infalling matter. Apart from these two effects, the Ly α flux around radio-loud objects can be enhanced due to interactions with the radio jets. The relatively fainter nebulae around radio-quiet QSOs compared to lobe-dominated radio-loud QSOs can be ascribed to this effect, or to significant differences in the environments between the two classes.

Key words. Galaxies: active – Galaxies: high-redshift – Quasars: emission lines

1. Introduction

Models of galaxy evolution require feedback mechanisms, e.g. from supernovae to regulate the star formation in order to reproduce galaxy luminosity functions (e.g. White & Frenk 1991). Recent simulations (Di Matteo et al. 2005; Springel et al. 2005) and semi-analytical models (Croton et al. 2006) have indicated that also a central active galactic nucleus can have strong effects on the surroundings. Such strong feedback mechanisms can be tested observationally by studying the environment of bright high redshift quasars, specifically by observations of the kinematics of extended gas.

In this paper we focus on observations of extended Ly α emission line regions (EELRs) surrounding $z > 2$ QSOs. Ly α EELRs are frequently found for radio-loud quasars (RLQ) (Heckman et al. 1991a). The Ly α emission nebulae are mostly

asymmetric around the lobe-dominated RLQs (Heckman et al. 1991b; Lehnert & Becker 1998), and the nebulae are aligned with the spatial orientation of the radio jets. Furthermore, these studies showed that the strongest line emission is mostly associated with the location of the stronger radio lobe. This alignment effect indicates some interaction of the radio emission and the EELRs through shocks. Radio galaxies, believed to contain obscured QSOs with the radio jet oriented closer to the plane on the sky than regular QSOs (Barthel 1989), are also found to have EELRs aligned with the radio emission (McCarthy et al. 1995). Besides these EELRs, which are possibly powered by jet interactions, radio galaxies at $z > 2$ are found to have more extended and quiescent Ly α halos with velocities around 500 km s^{-1} (Villar-Martín et al. 2003).

EELRs have also been reported around radio-quiet quasars (RQQs¹), typically based on long-slit spectra of a few indi-

* Based on observations obtained at the German-Spanish Astronomical Center, Calar Alto, operated by the Max-Planck-Institut für Astronomie Heidelberg jointly with the Spanish National Commission for Astronomy.

¹ In this paper the term QSO is used as a broad term that combines all types of quasars in one category. When the radio flux is specifically used to distinguish between radio-loud and quiet QSOs, the term RLQ or RQQ will be used.

vidual objects (Steidel et al. 1991; Bremer et al. 1992; Fried 1998; Møller et al. 2000; Bunker et al. 2003; Weidinger et al. 2004), or based on narrow-band images (Bergeron et al. 1999; Fynbo et al. 2000). The EELRs around RQQs need to be explained by effects other than interactions with jets, and possible explanations include the ionising radiation from massive stars in the host galaxy or from the AGN itself. Although the majority of quasars are radio-quiet, the phenomenon of extended emission around RQQs at high redshifts has not been studied systematically. From a larger sample of 12 QSOs, Hu & Cowie (1987) only found extended emission from one object, which suggests that the phenomenon is not common. Other investigations have reported companion Ly α emitting objects at the QSO redshifts that may be influenced by the QSO ionising radiation (Hu et al. 1996; Petitjean et al. 1996).

Apart from the feedback effect which will cause an outflow of the surrounding material, infalling matter also can be responsible for the observed Ly α photons. In a scenario where matter is falling into a potential well, Ly α photons are created via cooling processes, and ionisation by a QSO can greatly enhance the brightness of the EELRs. In a model of infalling material, Haiman & Rees (2001) predict that Ly α emission should be detectable in a region of $\sim 3''$ around QSOs, equivalent to ~ 25 kpc at $z \approx 3$, and with a typical surface flux density of $10^{-16} - 10^{-18}$ erg cm $^{-2}$ s $^{-1}$ arcsec $^{-2}$. Weidinger et al. (2004, 2005) found observational support for this interpretation by suggesting that the emission from the QSO is directed in a cone. However, studies of spatially extended Ly α emission line regions have failed to answer the question whether the emitting gas is infalling or outflowing.

This paper presents a study of seven QSOs at $2.7 < z < 4.5$ to look for narrow ($\lesssim 1000$ km s $^{-1}$) Ly α emission lines at the QSO redshifts. Because the spatial location of Ly α emission at the QSO redshift is not known in advance and can be highly asymmetric, integral field spectroscopy (IFS) is useful to locate the brightest EELRs. Previous IFS studies of EELRs around RLQs have focused on optical emission lines from low redshift objects (e.g. Durret et al. 1994; Crawford & Vanderriest 2000; Sánchez et al. 2004; Christensen et al. 2006), or the analysis of a single radio galaxy (Villar-Martín et al. 2005). IFS is well suited for this purpose because of the possibility to create narrow-band images at any suitable wavelength with an adjustable band width, and to simultaneously investigate velocity profiles.

This paper is organised as follows. Sect. 2 describes the data reduction, and Sect. 3 the analysis of the IFS data, with more detailed information on each object and the velocity structure of the EELRs. We explore scaling relations between the EELRs and the QSO luminosities in Sect. 4, and discuss these in Sect. 5. The conclusions are presented in Sect. 6. Throughout the paper, we assume a flat cosmology with $\Omega_\Lambda = 0.7$ and $H_0 = 70$ km s $^{-1}$ Mpc $^{-1}$.

2. Data set

The observations were performed with the Potsdam Multi Aperture Spectrophotometer (PMAS; Roth et al. 2000, 2005), mounted on the 3.5m telescope at Calar Alto during several

observing runs in the period 2002–2004. The study was carried out in connection with a different programme to study emission from Damped Ly α absorbers (e.g. Christensen et al. 2004). The sample consists of seven objects where the QSO Ly α line lies within the spectral window. The redshifts of the damped systems were different to the QSO redshifts and therefore Ly α emission lines detected at the QSO redshifts are clearly related to the QSO environments. No attempts were made to construct a complete or unbiased sample with respect to QSO properties, and the sample contained one flat spectrum, core-dominated RLQ and six RQQs at $2.7 < z < 4.5$ as listed in Table 1. Furthermore, only observations of the 4 lowest redshift objects covered the wavelength of C IV $\lambda 1549$ at the QSO redshift. Because of varying conditions, the total integration times for each object were adjusted to give the same signal-to-noise levels in the data cubes. A log of the observations is given in Table 2.

A detailed description of the data reduction and analysis is presented along with the Damped Ly α absorber study (Christensen 2005, ; Christensen et al., 2006, in prep). In summary, after the data reduction each observation of the QSO was contained in a data cube of spatial dimensions of $8'' \times 8''$ with a contiguous sampling. The data cube had 16×16 spatial elements (“spaxels”) where each spaxel covered a square of $0''.5$ on a side. The spectral range covered was from 1500 to 3000 Å, and a spectral resolution of 3 and 6 Å was obtained for the two setups used. The wavelength calibration was done in the standard manner using exposures of emission line lamps. Errors in the wavelength calibration in the final data cubes were estimated from strong sky emission lines indicating typical uncertainties of 0.3 Å. Flux calibrations used standard procedures by observations of spectrophotometric standard stars at the beginning and the end of each night.

3. Analysis

This section describes the processes to detect EELRs in the data cubes, and notes for each individual object. A more detailed analysis of the two brightest nebulae is also presented.

3.1. Subtracting the QSO emission

Since the QSO continuum and broad-line nuclear Ly α emission was by far the dominating contribution to the overall luminosity at rest-frame wavelength of 1215 Å, a subtraction of the nuclear emission was essential in order to search for a possible quiescent Ly α EELR around the nucleus. To give an idea of the extension of the PSF, the broad emission lines could be found even at a radial distance of $3''.5$ from the centers of the brightest QSOs. A visual inspection of the data cubes without the nuclear contribution subtracted gave no clear indication of the presence of such EELRs. Extended continuum emission from stars in the host galaxies is not expected to be measurable at this angular resolution (c.f. Jahnke et al. 2004). Three different methods for subtracting the QSO emission were investigated.

The simplest method to study EELRs uses conventional narrow-band filters to observe an emission line and the continuum adjacent to the line. Exactly the same procedure can

(1) Coordinate name	(2) Alt. name	(3) z_{em} (ref)	(4) z_{em} (cube)	(5) mag. (cube)	(6) seeing	(7) exposure time (s)	(8) class
Q0953+4749	PC 0953+4749	4.457	–	$R=20.0$	1.0	16200	RQQ
Q1347+112		2.679	2.679	$V=18.7$	0.6	12600	RQQ
Q1425+606	SBS 1425+606	3.17	3.203	$V=16.5$	1.0	10800	RQQ
Q1451+1223	B1451+123	3.246	3.261	$V=18.6$	0.8	12600	RQQ
Q1759+7539	GB2 1759+7539	3.050	3.049	$V=17.0$	1.2	12600	RLQ
Q1802+5616	PSS J1802+5616	4.158	–	$R=20.7$	1.0	27000	RQQ
Q2233+131		3.298	–	$V=18.3$	0.7	18000	RQQ

Table 1. List of observed QSOs. Redshifts for the QSOs reported in the literature (Column 3) are compared to the redshift determined from the IFS data cube (Column 4). The ‘–’ signs correspond to data where we could not reliably determine the QSO redshift from the emission lines in the IFS data cubes. Redshifts are derived from the vacuum corrected wavelengths. Column 5 gives the QSO magnitudes in the Vega system, and column 6 the seeing in arcseconds measured in the data cubes. Column 7 lists the total integration time and the last column is the class of object defined from radio observations.

QSO	date	exposure time (s)	grating	λ coverage (Å)	seeing	conditions
Q0953+4749	2004-04-16	4×1800	V300	3630–6980	0.9	stable
	2004-04-21	5×1800	V300	3630–6980	1.0	non phot.
Q1347+112	2004-04-20	7×1800	V300	3630–6980	0.6	non phot.
Q1425+606	2004-04-19	6×1800	V300	3630–6750	1.0	stable
Q1451+1223	2004-04-17	7×1800	V300	3630–6980	0.8	non phot.
Q1759+7539	2004-04-21	7×1800	V300	3630–6980	1.0–1.5	non phot.
Q1802+5616	2003-06-18	2×1800	V600	5100–6650	1.0	non phot.
	2003-06-20	3×1800	V600		1.0	non phot.
	2003-06-21	4×1800	V600		1.8	non phot.
	2003-06-22	6×1800	V600		0.9	stable
Q2233+131	2003-08-24	6×1800	V600	4000–5600	0.6	stable
	2003-08-25	4×1800	V600		0.7	non phot.

Table 2. Log of the observations. The last two columns show the average seeing during the integrations and the photometric conditions, respectively.

be used for the data cubes, with the advantage that we are free to choose a suitable wavelength range for both the on- and off bands. Since the redshift of quiescent Ly α emission was previously unknown, the central wavelengths and widths for the on-band images were determined from the emission lines found using the two other methods described below. The spectral range used to produce the offband images were the same as for the on-band images, but redwards by about 10 Å. This ensured that the nuclear line and continuum emission was removed, and produced narrow-band images of the quiescent component of the EELRs. The left hand panels in Fig. 1 show such residual narrow-band images centered on the wavelengths where narrow Ly α emission lines were found. The peak intensities were determined by fitting two-dimensional Gaussian functions in the on- and off-band images. Then the off-band image was scaled to the on-band peak and subtracted to create pure EELR images.

Another method takes advantage of the fact that the spectrum of a point source is the same, although scaled, in adjacent spaxels. From each reduced data cube a one-dimensional QSO spectrum was created by co-adding spectra from sev-

eral fibres within a 2'' radial aperture centered on the QSO. For each spaxel we determined a scale factor between the total one-dimensional QSO spectrum and each individual spaxel in an interval bracketing the QSO Ly α emission line and subtracted it from the initial spectrum. To a first approximation this process created a data cube that retained the EELR. To refine the process of finding pure emission lines, this residual emission line cube was subtracted from the original cube to create a cube with the QSO emission only. A new one-dimensional QSO spectrum was created, scaled to each spaxel and subtracted, again from the original data cube. The process was iterated until stable solution was found which occurred usually after 3 iterations only. After these 3 iterations, the total flux of the EELRs extracted from the residual spectra was found not to change with further iterations.

In the residual data cube, we analysed the spectra in the EELR and determined the spectral $FWHM$ of the emission lines shown in the left hand panels in Fig. 1. To find these widths, one-dimensional spectra associated with the emission lines were created first. Then images of the EELRs were created by choosing band widths corresponding to twice the mea-

sured *FWHM* of the emission lines and centered on the Ly α emission wavelength. More adjacent spaxels were added to the one-dimensional spectra if they showed up as bright points in the narrow-band images. This process was iterated interactively using the Euro3D visualisation tool (Sánchez 2004). Typically for the fainter objects, apertures of 1''.5 in diameter was used, which correspond to about 10 spaxels. For the brighter objects (Q1425+606 and Q1759+7539) a much larger aperture was used, and the one-dimensional spectra present a sum of 60 spaxels.

The third method used a technique of modeling the two-dimensional QSO image PSF in each monochromatic slice (e.g. Wisotzki et al. 2003; Sánchez et al. 2004; Sánchez et al. 2006). First, a two-dimensional model of the QSO PSF is made for each monochromatic slice in the data cube. By fitting two-dimensional Gaussian functions to these images we determine the spatial location, and the *FWHM* in x- and y directions of the QSO emission. Since these parameters vary smoothly with wavelength, we can use this information to make a model PSF in the form of a data cube. This model data cube is subtracted from the original data to create a residual data cube.

Qualitatively, the three methods gave the same impression about the presence and morphology of the EELRs, but each method had its advantages and drawbacks. The on-off band subtraction procedure was used to create the images in Fig. 1, but since this procedure accounted for one band only, we could not use this technique to analyse the spectra associated with the emission, which is the true advantage of IFS. Therefore, this method was only used to verify that the images derived from the more complex procedures were reproduced.

Comparing the results from the PSF scaling and the spectral scaling methods we found that the spectral properties, e.g. emission line fluxes and widths, were similar, but that significantly larger QSO residuals were present for the first method. Hence we decided to use the spectral scaling method for further analysis, unless noted otherwise. The difference between the two methods will be demonstrated in Sect. 3.2.5. A probable reason for the larger residuals from the PSF subtraction was the fact that the PSF could not adequately be described by a simple analytical function. On the other hand, when we analysed one single object (i.e. a point source) with a well known spectrum similar in every single spaxel, the spectral scaling method provided better results. However, in the case that the EELR have strong, point source like emission directly in the line of sight to the QSO, we probably over-subtracted the extended emission. In such a case, none of the procedures would be able to reconstruct the emission.

3.2. Notes on individual objects

In this section the results are presented in detail for each individual object, and much of the description refers to the images and spectra in Fig. 1. Non-photometric conditions during the observations or intrinsic variability of the QSOs make it difficult to determine whether spectrophotometric results were obtained. The absolute flux calibration uncertainties are estimated to be $\sim 20\%$ on the basis on comparing the spectrophotometry

with broad band magnitudes for the quasars reported in the literature. We cannot disentangle any absolute magnitude differences from the intrinsic flux variability of the QSOs though.

3.2.1. Q0953+4749

Only the QSO Ly α and Ly β emission lines are included in the spectral window and both are affected heavily by absorption lines in the Ly α forest. Hence no attempt is made to estimate the QSO redshift from the data cube.

The on-band image in Fig. 1 for Q0953+4749 corresponds to 6656–6682 Å. We find extended narrow Ly α emission at 6670 Å mostly towards the south of the QSO. This wavelength is redshifted by ~ 1000 km s $^{-1}$ relative to the QSO redshift. The existence of asymmetric emission extending over 5'' was found in a deep long-slit spectrum by Bunker et al. (2003). The signal-to-noise level in the data cube is too low to investigate the dynamics and morphology of this emission line region or to trace the emission over 5''. Apparently the brighter part of the emission in Fig. 1 extends over more than 2'' in the data cube.

3.2.2. Q1347+112

The narrow-band image for Q1347+112 corresponds to 4466–4482 Å. Ly α emission from this QSO appears in a region of the CCD affected by a bad column, which after QSO subtraction causes a distinct structure extending over the field in a narrow-band image. This can be seen to the north-west of the QSO center in Fig. 1. The emission line coincides with a sky emission line from which sky-subtraction residuals can be interpreted as narrow emission lines. Nonetheless, faint extended emission appears to be present, but further analysis is not possible.

3.2.3. Q1425+606

The narrow-band image for Q1425+606 corresponds to 5099–5122 Å. To estimate the QSO redshift a Gaussian function is fit to the O I $\lambda 1302$ emission line with $z_{\text{em}} = 3.2030 \pm 0.0008$. This is somewhat higher than $z = 3.17$ reported in the literature, which we also derive from the C II $\lambda 1335$ and C IV $\lambda 1549$ lines in the data cube. As a reference we use $z_{\text{em}} = 3.203$ because the O I line is a more reliable redshift indicator (Tytler & Fan 1992).

Q1425+606 has one of the brightest EELR in the sample, as shown in Fig. 1, and it is also the brightest QSO in the sample. It has large QSO subtraction residuals, but these are at a level consistent with Poissonian statistics. Any narrow Ly α emission that may be present within a radius of 0''.5 from the QSO center is heavily affected by these subtraction residuals, hence we do not recover the structure of the nebula here.

The Ly α emission is clearly asymmetric with most of the emission coming from a region to the south-east of the QSO. Co-adding spaxels in the region where the narrow Ly α emission is brightest gives a spectrum with a Ly α emission line with a total line flux of $(7 \pm 1) \times 10^{-16}$ erg cm $^{-2}$ s $^{-1}$.

Subtracting the QSO emission around the C IV line reveals no emission line in either the narrow-band image or one-

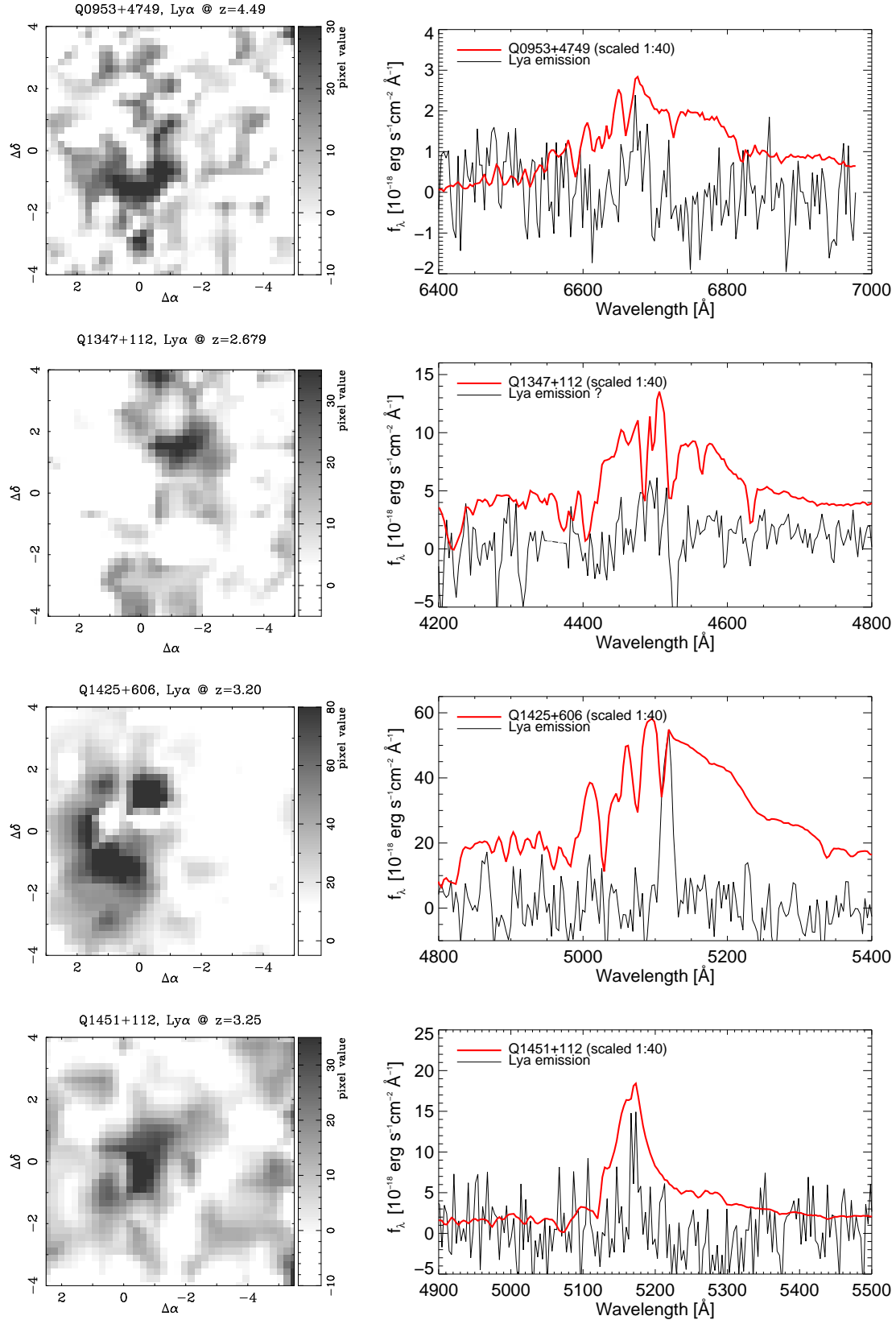


Fig. 1. Extended Ly α emission line regions at the QSO redshifts. The left hand panels show $8'' \times 8''$ narrow-band images created using a simple on-band minus off-band image technique. The centers of the QSOs are placed at the coordinates (0,0). All images are interpolated representations with pixel sizes of $0''.2$ with the orientation north up and east left. The bright objects (Q1425+606 and Q1759+7539) have strong residuals within the central $1''$. The Right hand panels show the spectra of the extended narrow Ly α emission (thin line) compared with the QSO spectra scaled down by a factor of 40 (thick line). The spectrum of Q1802+5616 was only scaled down by a factor of 3. No extended emission is found from Q1802+5616 and Q1347+112. Where found, the Ly α emission lines from the EELRs are clearly narrower than the broad QSO lines.

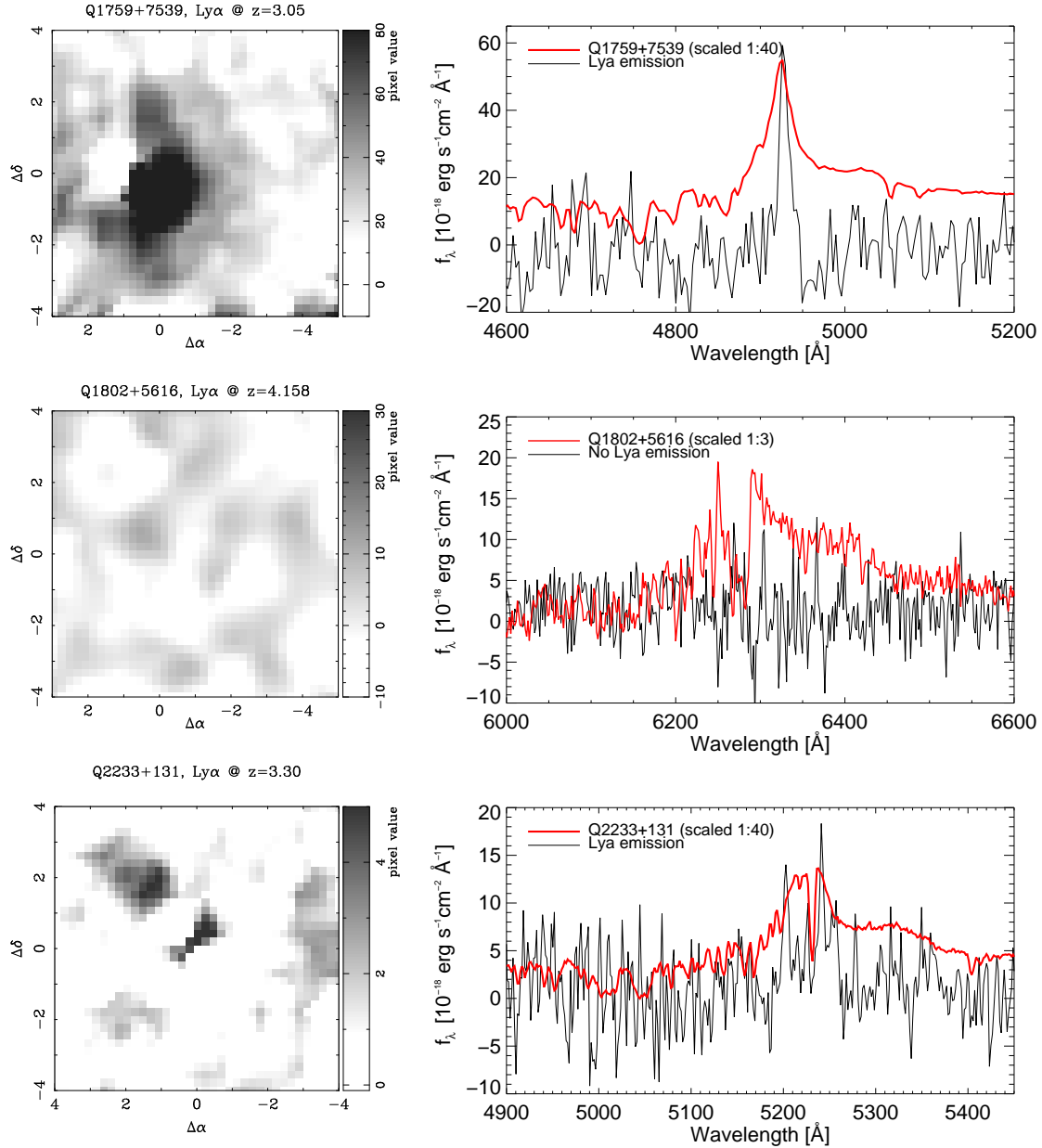


Fig. 1. *continued.*

dimensional spectrum. We derive a 3σ upper detection limit of 6×10^{-17} erg cm $^{-2}$ s $^{-1}$.

3.2.4. Q1451+112

The narrow-band image for Q1451+112 corresponds to 5163–5173 Å. The broad QSO Ly α emission line is strongly affected by absorption lines in the Ly α forest. An estimate of the QSO redshift is difficult because the red wing of the O I $\lambda 1302$ line is affected by residuals from the 5577 Å sky line. However, we adopt $z = 3.261$ estimated from this emission line. A lower redshift of $z = 3.2468$ is inferred from the C IV $\lambda 1549$ line.

After QSO spectral subtraction a faint narrow emission line region is found extending to $\sim 2''$ to the north-west and west of the QSO as seen in Fig. 1. This narrow emission line has

$z = 3.2530$ implying a velocity difference of $+700$ km s $^{-1}$ relative to C IV from the QSO broad line region but a blue shift of -600 km s $^{-1}$ relative to the O I line. Further analysis of the structure of the emission line region is not possible with the signal-to-noise level in the individual spaxels.

3.2.5. Q1759+7539

The narrow-band image for Q1759+7539 corresponds to 4919–4933 Å. This object is the only RLQ in the sample with a core-dominated, flat-spectrum radio emission (Hook et al. 1996), and like Q1425+606 it is also very bright in the optical. A Gaussian fit to the QSO C IV emission line gives $z = 3.0486 \pm 0.0008$, where the error includes the wavelength calibration error. The Ly α emission line gives a similar result;

other emission lines are fainter or do not allow for a good determination of the redshift because absorption lines affect the line profiles. The on-off band image in Fig. 1 shows the clear presence of an extended structure to the south-west of the QSO center.

The two different methods for the QSO PSF subtraction were investigated in more detail. Modeling the QSO PSF as a function of wavelength gives a narrow-band image very similar to that in Fig. 1. However, we find that the spectrum is much noisier as demonstrated in Fig. 2. Most importantly, we find that the total flux in the extracted one-dimensional spectrum remains the same within the uncertainties.

As for Q1425+606, we do not find extended C IV emission from this object either, with an upper limit of 9×10^{-17} erg cm $^{-2}$ s $^{-1}$.

3.2.6. Q1802+5616

The narrow-band image for Q1802+5616 corresponds to 6270–6277 Å. No Ly α emission line nebula is found at the QSO redshift, but this is possibly because the QSO itself is fainter than the others in this sample. The QSOs continuum emission is \sim 40 times fainter than for the two bright QSOs in our sample. Thus if any correlation between the QSO and EELR flux is present, the narrow Ly α EELR should have a total flux of 3×10^{-17} erg cm $^{-2}$ s $^{-1}$ which is below the detection limit in this data cube. This flux has been estimated applying a global scaling relation between the QSO emission and the EELR flux as detailed in Sect. 4. Because the QSO Ly α emission line falls close to the strong sky emission line at 6300 Å and is affected by strong residuals, this object is not considered further here.

3.2.7. Q2233+131

The narrow-band image for Q2233+131 corresponds to 5223–5230 Å. Only the broad Ly α emission line lies within the spectral range in the data cube, and this line only is insufficient to estimate the QSO redshift. The broad Ly α line is affected by both Ly α forest lines and a strong Si II λ 1260 absorption line associated with a DLA system (see Christensen et al. 2004). Since no adequate redshift could be determined from the data cube, we rely on the literature value for the QSO redshift.

After QSO subtraction we find an emission line object 1'' to the north-east of the QSO. The scaled spectrum subtraction method reveals a region that appears to have an emission line at 5227 Å which is at the same wavelength as the Si II absorption line in the QSO spectrum. In contrast the PSF subtracted cube also shows an emission region to the north-east, but the associated emission line is at 5240 Å, i.e. shifted by 700 km s $^{-1}$ relative to the QSO redshift. In the case of the scaled spectrum subtraction, an inaccurate wavelength calibration could introduce a shift in the wavelength of the emission line due to the presence of the absorption line, while this is not the case for the PSF subtraction. Therefore Fig. 1 and Table 3 present the results from the PSF subtraction technique. To the limit of detection this region does not appear to be very extended.

3.3. Velocity structure

We now proceed with a more detailed investigation of the velocity structures and morphologies for the two brightest nebulae.

We start with the emission line nebula around Q1425+606. For each spaxel we fit a Gaussian profile to the spectrum around the expected position of the Ly α line using `ngaussfit` in IRAF. After an automatic fit to all spectra in the cube, the fit of each individual spectrum is checked interactively. No constraints on the parameters in the fits are imposed. These fits are used to estimate for each spaxel the line flux, centroid and *FWHM*. The *FWHM* is corrected for instrument resolution before deriving the velocities. Results from these fits are shown in Fig. 3 and are presented as maps that retain the individual spaxels rather than the interpolated images shown in Fig. 1. Only spaxels that have sufficient signal to allow for a visual detection of an emission line are included. The upper left panel shows the relative velocity offsets where as a reference point we use the QSO redshift $z_{\text{em}} = 3.203$. We find evidence for velocities of \sim 600 km s $^{-1}$ close to the QSO decreasing to 100–200 km s $^{-1}$ at a distance of 3''.5 from the QSO. In projection this corresponds to \sim 25 kpc. Using the redshifts inferred from the C IV and C II lines implies velocity offsets of \sim 3000 km s $^{-1}$ at the center.

The surface brightness of the Ly α emission ranges from 2×10^{-16} erg cm $^{-2}$ s $^{-1}$ arcsec $^{-2}$ close to the QSO to about 2×10^{-17} erg cm $^{-2}$ s $^{-1}$ arcsec $^{-2}$, 3'' from the QSO. After correcting the measured *FWHM* for the average instrumental resolution, we find typical line widths of 10–15 Å corresponding to a velocity dispersion of 600–900 km s $^{-1}$ as illustrated in the lower left panel. The *FWHM* is slightly lower to the south of the QSO (300 km s $^{-1}$). There are indications of a high velocity dispersion closer to the QSO, but the uncertainty is high in this region due to QSO PSF subtraction residuals. In the upper right panel in Fig. 3 we show the flux in each spaxel overlayed by velocity contours. The lower right hand panel in Fig. 3 shows the one-dimensional trace of the velocity offset and Ly α surface brightness distribution as points connected by solid and dashed lines, respectively. These profiles are derived at PA = 135° east of north where the emission line region appears to have the largest extension. Fluxes and velocities at each point are derived from an average of four spaxels. The uncertainties are estimated from the standard deviations of these four values which are combined in quadrature with typical uncertainties for a single spaxel. The surface brightness profile has an exponential scale length of \sim 2''.5 which corresponds to 20 kpc at the QSO redshift.

Maps of the velocity structures of the Ly α nebula around Q1759+7539 are presented in Fig. 4. The surface brightness shows bright parts to the south-west of the QSO, but also to the east some fainter emission appears. However, this is not clearly visible in the on-off band image in Fig. 1. Including the eastern part of the nebula, the total extension of the nebula appears to be about 8'' along the longest axis. Considering the bright part of the nebula along PA = 225°, the velocity profile is consistent with a slope of zero within 1 σ uncertainties. The interpretation is difficult because of the complex velocity structure in the

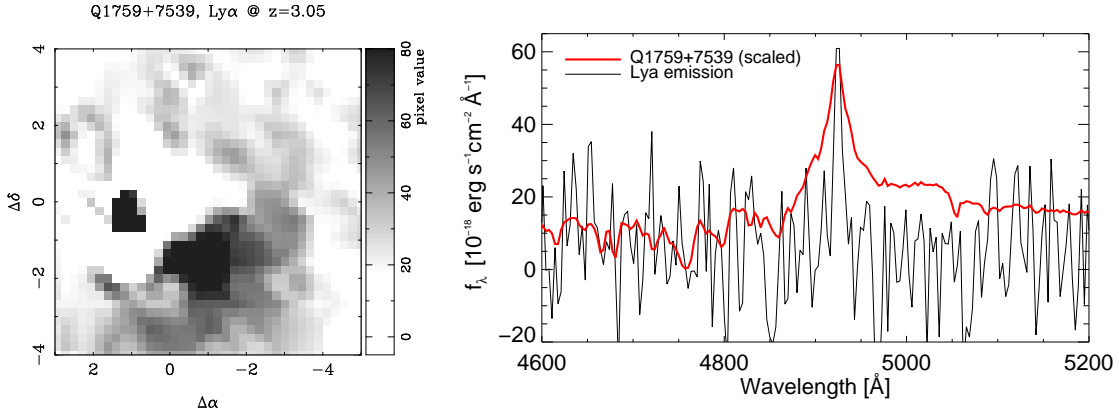


Fig. 2. Similar to Fig. 1, but using an alternative QSO subtraction method, where the PSF is modeled as a function of wavelength. The image still shows strong residuals close to the QSO center. Compared to the spectrum in Fig. 1, the one-dimensional spectrum of the EELR is more noisy.

nebula as shown by the contours in the upper right panel. This is also the case for the $FWHM$ in the lower left panel, but it appears to be constant within errors at $\sim 450 \text{ km s}^{-1}$ in the bright part of the nebula. The eastern part of the nebula shows similar velocity offsets of $200 \pm 150 \text{ km s}^{-1}$ relative to the QSO redshift but the $FWHM$ is significantly larger: $> 1100 \text{ km s}^{-1}$.

The surface brightness profile has an exponential scale length of $1''.4$ corresponding to $\sim 10 \text{ kpc}$. This is smaller by a factor of two compared to the value estimated for the Q1425+606 nebula.

4. Results

We detect extended Ly α emission for 5 of the 7 systems. It is possible that all 7 QSOs have extended emission, but one QSO is too faint, and the other is affected by a CCD defect at the wavelength of interest. Table 3 lists the flux, $FWHM$ and extension for each detected EELR. Fluxes are corrected for galactic reddening using the dust-maps of Schlegel et al. (1998). Compared to the broad Ly α emission lines from the QSO broad line region, which have velocities around 10000 km s^{-1} , the nebulae have much narrower Ly α emission lines ($\sim 500 \text{ km s}^{-1}$). The emission appears to be asymmetric and mostly one-sided, and the brightest extended Ly α emission nebulae are found around the brightest QSOs.

Only for the two brightest objects can the surface brightness be measured. The angular sizes of the brightest two nebulae are measured along the long axis. For the fainter Ly α emission regions the extension is estimated by the offset between the QSO centroid and the most distant emission seen in the IFS data. Errors of these values are comparable to the spaxel size, which at the QSO redshifts sample approximately 5 kpc. The uncertainties for the velocity offsets listed in column 9 are mainly caused by uncertainties in the wavelength calibration leading to uncertainties in the derived redshifts of $\Delta z \approx 0.0005$. Velocity offsets are derived from the emission lines in the one-dimensional spectra, and therefore can differ from the velocities derived from the analyses of the kinematics in Sect. 3.3.

4.1. Emission line fluxes

How much flux is emitted by the EELRs compared to the overall flux of the QSOs themselves? The scalings of the spectra shown in Fig. 1 could indicate some relation. To estimate the flux in the IFS data, we integrate the extended narrow-Ly α flux in the nebulae from Gaussian fits to the one-dimensional spectra. To calculate the flux from the QSOs in the same wavelength interval we integrate the one-dimensional QSO spectra from -10 Å to $+10 \text{ Å}$ centered on the narrow Ly α emission wavelength, and correct for Galactic extinction as well. We find that the flux densities in the EELRs represent approximately 1–2% of the QSO fluxes within the narrow-band filter.

This fraction is much lower than that commonly found for RLQs. In a narrow-band imaging study of high redshift steep-spectrum, lobe-dominated RLQs, Heckman et al. (1991b) (hereafter H91b) found that extended Ly α emission is a common feature around these objects. The Ly α EELRs contained a flux fraction of $\sim 10\text{--}25\%$ that of the QSOs within the filter width of 15 Å in the H91b sample. The narrow-band Ly α flux from the QSOs spans the same range in the two samples, but our data have Ly α EELR fluxes approximately an order of magnitude smaller than the H91b sample. The band width of 20 Å that we choose corresponds roughly to the same rest-frame band width for a $z = 3.2$ system as a 15 Å wide band at $z = 2.2$, which is the median redshift in the H91b sample. Hence the two samples are directly

H91b also estimates that the flux in the EELRs corresponds to about 10% of the flux in the broad line region of the QSO taking into account the flux falling outside the narrow-band filter. Likewise, if we integrate the broad line Ly α flux from the one-dimensional QSO spectra, we find that the EELRs contain around 0.5% of the flux relative to the QSOs.

The median spatial extension in the H91b sample is $11''$ (or 90 kpc in the adopted cosmology), which is significantly larger than the extensions found here. The two brightest objects have extensions of $\sim 4''$ or $\sim 30 \text{ kpc}$ at $z \approx 3$. The sensitivity in the Heckman et al. (1991b) study is $1 \times 10^{-17} \text{ erg cm}^{-2} \text{ s}^{-1} \text{ arcsec}^{-2}$, which is about a factor of two better than that reached by our IFS observations. Because of the

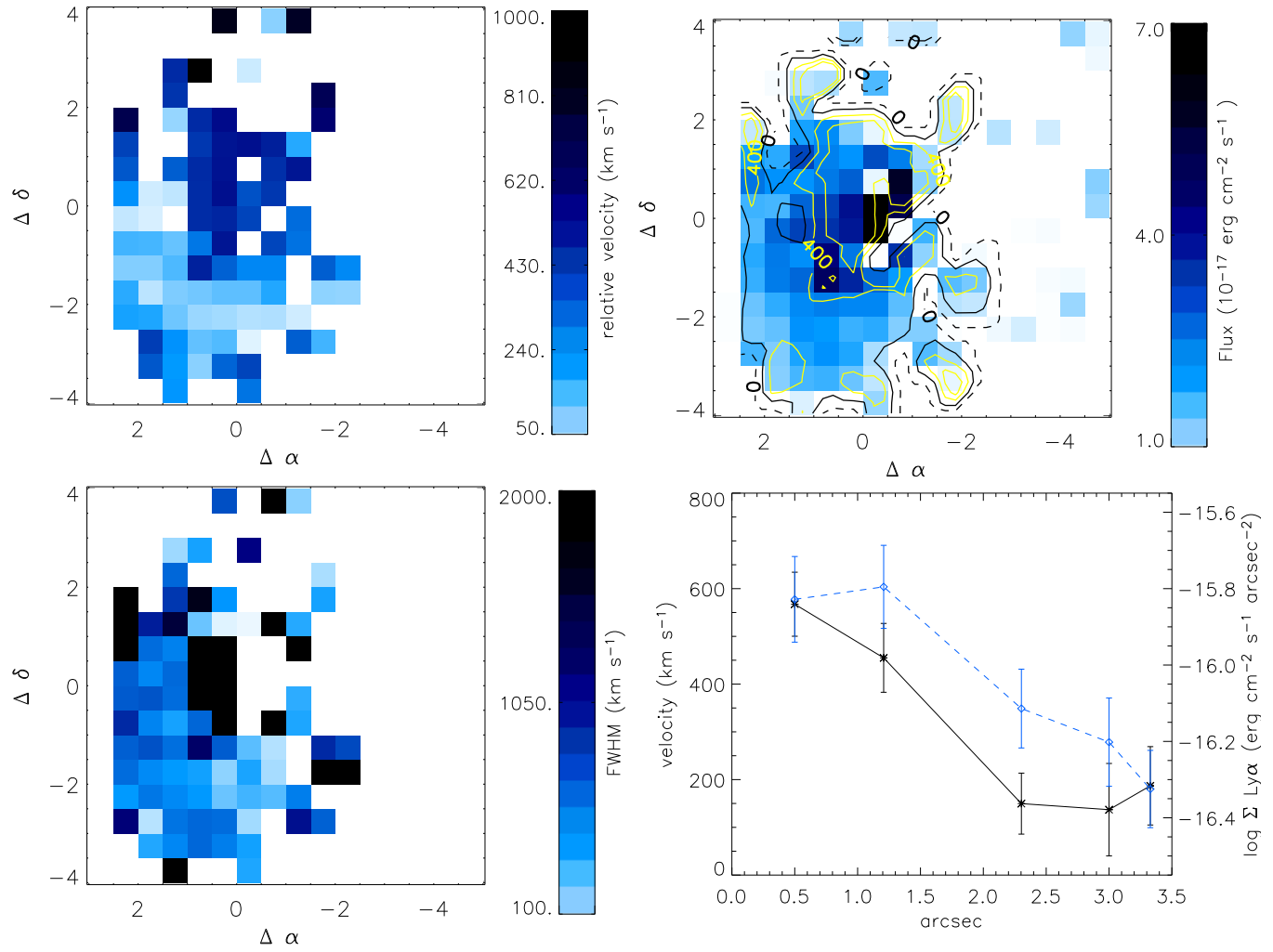


Fig. 3. Maps of properties for the Ly α emission nebula around Q1425+606. *Upper left panel:* Map of the Ly α emission velocity offset relative to the QSO redshift. *Upper right panel:* Map of the integrated flux from each spaxel with smoothed velocity contours overlaid. White fields correspond to spaxels where the Ly α emission line could not be recognised visually, which therefore warps the velocity contours close to the QSO center at (0,0) where residuals are present. *Lower left panel:* Map of the Ly α FWHM corrected for the instrument resolution. The *lower right panel* shows the radial profiles of the velocity component (solid line, left side axis) and Ly α surface flux density (dashed line, right axis) starting from the center of the QSO along a direction with PA = 135° east of north. A fit of the radial surface brightness profile by an exponential function gives a scale length of $\sim 2''5$ (20 kpc). [See the online edition of the Journal for a colour version of this figure.]

cosmological dimming of $(1 + z)^4$, the redshift difference between the two samples has an effect on the observed extension of the nebulae emission. The H91b sample has a median redshift of 2.2, and their data therefore reach a factor of $(1 + 3.11)^4 / (1 + 2.2)^4 = 2.7$ fainter than ours (mean redshift 3.11). Thus, the extension of the Ly α nebulae around the RQQs could be 50% larger if the surface density profile is extrapolated to larger radii. Even if we take into account this effect from the redshift differences, and assume that the surface brightness profiles can be extrapolated, the EELRs around RQQs have smaller sizes than those around RLQs.

4.2. Emission line luminosities

Instead of the measured fluxes, we investigated whether the redshift difference between the two samples has an effect and calculate the luminosities for the given cosmology. For a given quasar luminosity, the total luminosities in the Ly α nebulae from RQQs are consistent with being 10 times fainter relative to those from RLQs.

In addition to the flux in the 20 Å narrow-band image, we investigate the fraction of the broad line region (BLR) line luminosity for the QSOs relative to those for the EELRs. To calculate the QSO Ly α fluxes, we subtract the underlying powerlaw spectrum of the QSO and integrate the one-dimensional spectra over the broad Ly α lines. The fluxes are corrected for Galactic extinction, and the luminosities are calculated. Fig. 5

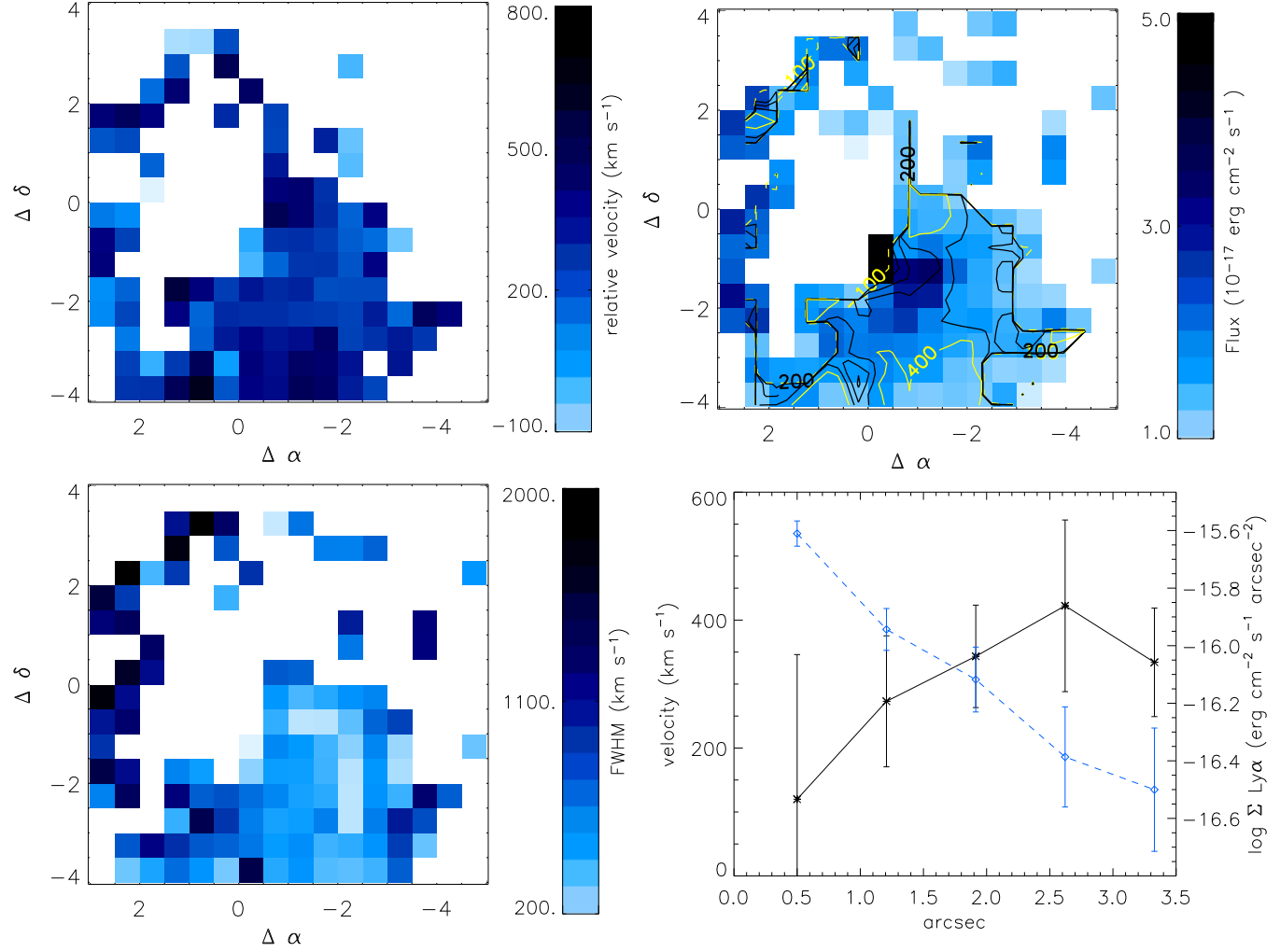


Fig. 4. Maps of the Ly α emission nebula surrounding Q1759+7539. The panels are similar to those described in Fig. 3. Profiles in the lower right panel are derived at PA = 225° east of north. A fit of an exponential function to the radial surface brightness profile gives a scale length of $\sim 1''.4$ corresponding to 10 kpc at the QSO redshift. [See the online edition of the Journal for a colour version of this figure.]

(1) Name	(2) z (Ly α)	(3) V (km s $^{-1}$)	(4) Σ (Ly α) (erg cm $^{-2}$ s $^{-1}$ arcsec $^{-2}$)	(5) size (kpc)	(6) f_{tot} (10 $^{-16}$ erg cm $^{-2}$ s $^{-1}$)	(7) $\log L_{\text{tot}}$ (erg s $^{-1}$)	(8) FWHM (km s $^{-1}$)	(9) ΔV (km s $^{-1}$)
Q0953+4749	4.489			13	0.36 ± 0.17	42.9	1000	1800 ± 200
Q1425+606	3.204	600–200	2×10^{-16}	34	9.8 ± 0.8	43.9	500	100 ± 100
Q1451+122	3.253			15	1.8 ± 0.5	43.2	500	-600 ± 100
Q1759+7539	3.049	200–300	3×10^{-16}	60	9.9 ± 1.6	43.9	450	0 ± 100
Q2233+131	3.301			10	1.1 ± 0.4	43.0	<400	700 ± 100

Table 3. Properties of the Ly α nebulae around the QSOs. Columns (1) list the names, (2) the redshifts derived from the narrow emission lines, (3) velocity offsets in the EELRs relative to the QSO redshifts, (4) peak surface brightness, (5) apparent extension of the Ly α nebula, (6) total Ly α flux from the nebula, (7) total luminosity in the nebulae, (8) Emission line FWHM corrected for instrumental resolution, (9) Relative velocity offsets between the narrow emission lines (one-dimensional spectra) and the QSO redshifts. Fluxes have been corrected for Galactic reddening. An analysis of the surface brightness has been attempted only for the two objects with very bright nebulae.

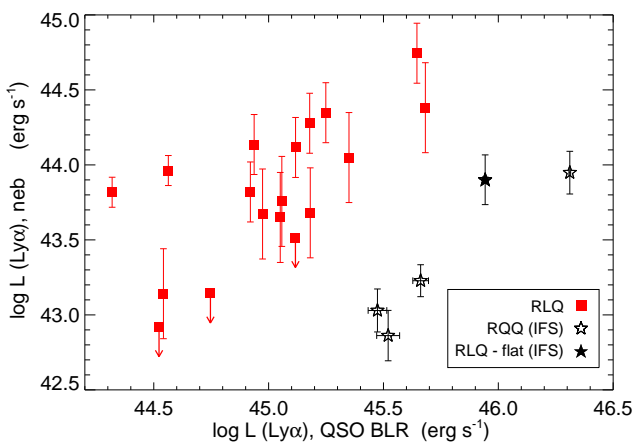


Fig. 5. Luminosities in the EELRs as a function of the integrated luminosities for the QSO broad Ly α lines. The IFS results are indicated by stars, where the filled star represents the one core-dominated RLQ, and the outlined stars the four RQQs. Squares represent the emission line nebulae surrounding 18 lobe-dominated RLQs from the sample in H91b. Arrows indicate upper limits for objects where no extended Ly α emission was found.

shows the luminosities of the nebulae as a function of the broad line region luminosities. The broad Ly α line fluxes for the RLQ are multiplied by a factor of 2 to account for the flux that falls outside the narrow-band images (see H91b). This figure shows that the luminosity of the EELR contain about 0.5% of the luminosities of the QSO broad Ly α lines.

Statistical tests support that there is a linear relation for the RQQs and the one RLQ from the IFS sample in Fig. 5. A Pearson test gives a correlation coefficient of 0.92 ± 0.04 for a linear correlation, where the error bar is derived by boot strapping techniques by adding random values corresponding to the uncertainties for the luminosities. Here the uncertainty of the QSO luminosities are assumed to be dominated by photon shot noise. A corresponding analysis for the RLQs gives a moderate linear correlation coefficient of 0.64 ± 0.06 , where the non detections in H91 are excluded. For the combined sample of 20 objects we find no obvious correlation, and a correlation coefficient of -0.04 ± 0.05 .

To test whether there is a factor of 10 difference between the luminosities of the Ly α nebulae for the two samples, the EELR luminosities from the IFS data are multiplied by 10. A Pearson test on the total sample then gives a correlation coefficient of 0.71. Hence, the simple statistical tests justify the qualitative description of the difference for the two samples given above.

It would be valuable to compare our study with the EELRs reported for RQQs in the literature, but these are mainly based on slit spectra. Therefore, a direct comparison cannot be done because the total flux in the EELRs could be underestimated because of slit losses. Nevertheless, the luminosity of one QSO and its Ly α EELR in Steidel et al. (1991) would place it very close to the two brightest objects in our IFS study in Fig. 5, and consistent with the proposed scaling. The narrow-band im-

age of Q1205–30 in Fynbo et al. (2000) and Weidinger et al. (2005) would place this object close to the faintest objects, and still consistent with the correlation. From a narrow-band image of one radio-weak QSO, Bergeron et al. (1999) report a Ly α EELR luminosity and extension similar to that of the RLQs however, the narrow-band magnitude shows that the QSO is very bright. We do not have sufficient information to evaluate whether the properties of this QSO are consistent with any of the scaling relations.

4.3. Quasar luminosities

To investigate whether the QSO ionising radiation has an effect on the fluxes and extension of the EELRs, we first estimate the continuum ionising flux from the QSOs. We take the U , B , or V magnitudes reported for the QSOs in the literature, and use a QSO template spectrum to calculate a K-correction between the observed band and the rest frame flux at 912 Å. The template spectrum is a hybrid of the Sloan Digital Sky Survey composite spectrum (Vanden Berk et al. 2001) and the composite FUSE spectrum (Scott et al. 2004). For Q0953+4749, its reported V band magnitude is heavily affected by absorption in the Ly α forest. At $z = 4.489$ the mean transmission in the Ly α forest is 0.33 (Songaila 2004), thus we adopt a correction of 1.2 magnitudes in addition to the K-correction. Most other quasars have magnitudes measured slightly redwards of the Ly α emission lines, or the transmissions bluewards of the Ly α lines are not as strongly affected at $z \approx 2$. Fig. 6 shows the luminosities of the extended Ly α emission line regions as a function of the predicted quasar luminosities at 912 Å. Symbol shapes are as in the previous figures. Taken at face value irrespective of the small number statistics, the RQQs are offset to brighter values, but this is a selection effect, because the quasars observed here are bright and at higher redshifts. The one RLQ in the IFS sample has properties similar to the RLQs in the H91b sample.

The figure suggests that the flux in the EELRs is independent of the nuclear ionising emission, which is perhaps contrary to the expectation. The same result is reached using K-corrections to estimate the luminosities at rest-frame 1450 Å, which shows that the results are independent of the specific point of reference. Even in the case that the ionising flux levels of the QSOs are estimated incorrect by a factor of two due to the uncertainty in the individual continuum levels relative to the template spectrum, this will not affect the conclusion.

The flux we observe is the unabsorbed fraction. Possibly the results are affected by dust extinction or absorption by neutral hydrogen in the QSO surroundings. An analysis of ~ 10000 QSO spectra have revealed that reddening affects only a few QSOs (Hopkins et al. 2004), and even very red QSOs show no evidence of dust obscuration (Benn et al. 1998).

QSOs do generally not have Lyman limit edges (Antonucci et al. 1989; Koratkar et al. 1992), which rules out significant amounts of hydrogen absorption. Of the five QSOs studied here, two have no breaks (Q0953+4749 and Q1425+606) and possibly also Q1759+7539, although our spectrum only reaches 3650 Å, i.e. 40 Å bluewards of the location of the break. The spectrum of Q2233+131 does not

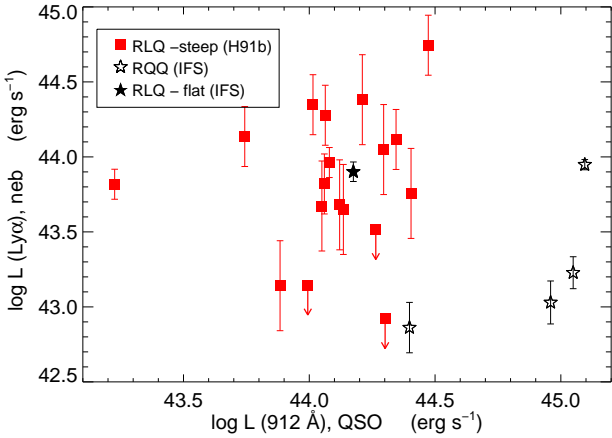


Fig. 6. Extended Ly α emission line luminosities as a function of the predicted quasar luminosities at the rest-frame 912 Å. There is no significant correlation between the EELR luminosities and the nuclear ionising luminosities.

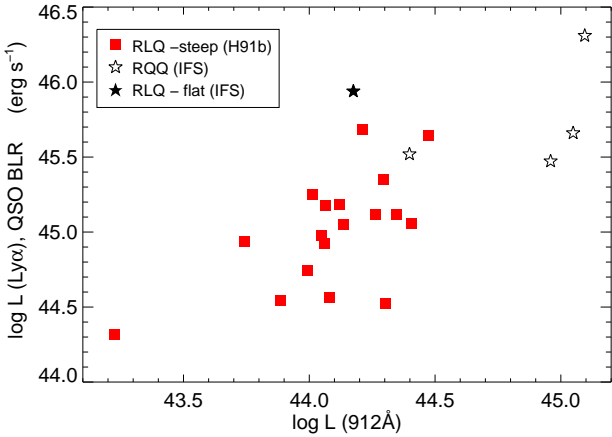


Fig. 7. Integrated luminosities from the QSOs broad Ly α lines as a function of the ionising flux calculated at 912 Å.

cover the break. Q1451+122 shows indication of a break at 3840 Å, i.e bluewards by 3000 km s $^{-1}$ from the QSO systemic redshift. This tells us that the absorption in the QSO lines of sight is not significant, but the absorption towards EELRs cannot be quantified with our data set. Assuming that the QSO sight lines are roughly representative for the absorption, we find that neither extinction nor absorption plays an important role.

Additionally we investigate how the quasar BLR Ly α fluxes correlate with the predicted quasar luminosities. As shown in Fig. 7 there appears to be a correlation that quasars with brighter 912 Å continuum emission also have brighter Ly α emission. The total sample has a correlation coefficient -0.72 ± 0.05 . Again Poissonian uncertainties are assumed and bootstrap tests used to derive errors. We will return to the correlations in Sect. 4.6.

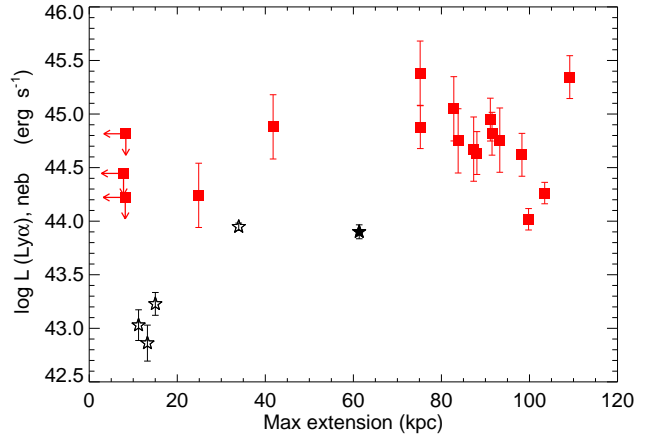


Fig. 8. Total Ly α luminosity from the nebulae as a function of the maximum projected sizes. Symbol shapes are as in the other figures and arrows indicate upper limits.

4.4. Ly α nebula extension

The median size in the H91b sample is ~ 90 kpc which is significantly larger than the ~ 30 kpc found for the brightest nebulae in the IFS data. Fig. 8 shows the total Ly α luminosity from the nebulae as a function of the apparent maximum projected angular size. Smaller nebulae have lower luminosities, whereas RLQs from H91b are larger and more luminous. A Pearson test on the distribution of luminosities relative to the sizes in the total sample gives a correlation coefficient of 0.44 ± 0.03 .

Morphologically there could be a difference between the RQQs and RLQs. For the RQQs in this IFS study we find evidence for one-sided emission only. Both one-sided emission (Weidinger et al. 2005) and two-sided Ly α emission (Møller et al. 2000) is reported for RQQs. In comparison, the Ly α nebulae around the RLQs are asymmetric, and in many cases two-sided emission is found (H91b). Similarly, the one core-dominated RLQ in Fig. 4 shows indications of emission on both sides of the QSO.

In the case of RLQ, the emission appearing asymmetric and two-sided could be explained by interactions of the jet with the ambient medium, since the brighter optical emission has been found aligned with the brighter radio emission (H91b). The asymmetry for the EELRs around RQQ must be explained by other means, for example by an intrinsic asymmetric distribution of material around the QSOs.

4.5. EELR cloud masses

Knowing the EELR luminosities and the Lyman continuum luminosity (at 1200 Å), it is possible to estimate the masses of the hydrogen clouds (Heckman et al. 1991b, equation 2c) $M \propto L_{\text{Ly}\alpha} U / Q M_\odot$. We assume that the ionisation parameter U is the same for the RQQs studied here. The Lyman continuum luminosity Q is larger by a factor of a few for the RQQ in our sample compared to the RLQ in H91b. Since the EELR Ly α luminosities of the RQQs are smaller by a factor of ~ 10 , it

follows that the masses of the EELRs around RQQ are at least a factor of 10 smaller than for RLQs, i.e. 10^7 – 10^8 M $_{\odot}$.

The same conclusion would be reached if we follow the arguments in Villar-Martín et al. (2003). Their equation to calculate gas cloud masses around radio galaxies combines the luminosity L , volume of the cloud V , and the filling factor f : $M \propto (LVf)^{1/2}$. It is difficult to estimate the volume of the clouds, but since the extensions are smaller for the RQQ, the volumes are too. Assuming a similar filling factor would lead to masses in the range 10^8 – 10^9 M $_{\odot}$.

4.6. General correlations for RQQ and RLQ

The treatment of the correlations of the properties described above avoided the upper limits measured for three of the RLQs. Here we use a generalised Kendall test (Isobe et al. 1986), which allows a treatment of limits as well. The total sample includes the 5 objects from our IFS data, and the 18 objects in the H91b study. Table 4 reports the probabilities for the null hypothesis that no correlation exists, i.e. small numbers are equivalent to high probabilities. Only correlations giving probabilities above 99% are considered as indications of a correlation. The purpose is to find which fundamental relations govern the observed properties of the emission line nebulae. For the tests we use the total Ly α luminosity in the EELRs ($L_{\text{Ly}\alpha,\text{neb}}$), the total flux from the QSOs in the broad Ly α line ($L_{\text{Ly}\alpha,\text{QSO}}$), the maximum extension of the Ly α nebulae (size), and the predicted quasar luminosities at the rest frame 912 Å ($L_{\text{QSO},912}$).

The probabilities listed in Table 4 are generally quite high which indicates that no correlation is present. Two exceptions exist. There is a probability of 99.7% for a correlation between the QSO Ly α luminosity and the luminosities at 912 Å.

Otherwise the luminosities at 912 Å do not show strong correlations with either nebulae sizes nor luminosities. This implies that the ionising fluxes from the QSOs do not directly affect the EELRs. If this is true, the main difference between the RLQ and RQQ should lie in the environment. The luminosity at 912 Å is uncertain due to the extrapolation of measured broad band magnitudes with a QSO template spectrum. We investigate this effect by multiplying the fluxes by a random factor between 0.5 and 2 and then applying the correlation tests. We do not find changes in the probabilities that significantly alter the conclusions.

The nebula sizes show the strongest correlation with the nebula Ly α luminosity with a probability of 99.9% for a correlation. This correlation implies that more luminous nebulae have larger sizes, which is also shown in Fig. 8.

5. Summary and discussion

We have presented evidence for differences in the extended Ly α nebulae around radio-quiet QSOs compared to radio-loud QSOs in the literature. We find that the brightest emission in these nebulae is around 2 – 3×10^{-16} erg cm $^{-2}$ s $^{-1}$ arcsec $^{-2}$ and extending to $\sim 4''$. Typical line widths are 500 km s $^{-1}$, and the lines are shifted between –600 and 1800 km s $^{-1}$ from the QSO systemic redshifts. The EELRs contain 1–2% of the QSO nuclear emission within the same pass band, or about 0.5% of

	$L_{\text{Ly}\alpha,\text{neb}}$	size	$L_{\text{QSO},912\text{\AA}}$
$L_{\text{Ly}\alpha,\text{QSO}}$	0.174 (0.403)	0.266 (–0.332)	0.003 (0.885)
$L_{\text{Ly}\alpha,\text{neb}}$...	0.001 (1.020)	0.594 (–0.158)
size	0.234 (–0.356)

Table 4. Generalised Kendall's test probabilities for the null hypothesis that no relation exists between any two given quantities. The sample includes the IFS objects and the RLQs in H91b. The values in brackets give the correlation coefficients. The observed properties involved here are: the total luminosity in Ly α in the EELRs ($L_{\text{Ly}\alpha,\text{neb}}$), the flux from the QSOs in the broad Ly α line ($L_{\text{Ly}\alpha,\text{QSO}}$), the maximum extension of the Ly α nebulae (size), the quasar luminosities estimated at the rest-frame 912 Å ($L_{\text{QSO},912\text{\AA}}$).

the flux of the integrated broad Ly α line from the QSOs. These are an order of magnitude smaller than found for RLQs studied in the literature (H91b). Similarly, the nebula sizes analysed here are a factor of a few smaller than detected around RLQs. Bremer et al. (1992) have suggested that the fainter EELRs around two RQQs were caused by a smaller covering factor of the neutral material relative to RLQs. Another interpretation is that the extended radio lobes, or alternatively the same process that creates these, is responsible for the main fraction of Ly α line emission in steep-spectrum, lobe-dominated RLQs.

Observations have shown that lobe-dominated RLQs have EELRs which are aligned but not exactly correlated in location with the lobes (H91b). Also optical emission line regions do not always show obvious alignment with the radio emission (Crawford & Vanderriest 2000). This suggests that the radio emission traces the direction of the AGN ionising cone, but that an interaction between the radio-jet and the environment is not necessarily the only cause. In some cases, jet interactions could dominate the observed properties of the EELRs. For RQQs the properties of the EELRs must be caused by a different mechanism. The radio emission is typically 2–3 orders of magnitude fainter than for RLQs. If an interaction with a faint radio jet was solely responsible for the Ly α nebulae in the RQQs, the Ly α emission would be much fainter than that observed.

The AGN unification scheme states that the different radio properties of radio-loud objects are related to their viewing angle (Barthel 1989), and core-dominated RLQs have jets very close to the sight line. Assuming that external conditions are similar for the two bright emission nebulae studied here, a difference in viewing angle is supported by the observed scale lengths in the surface brightness profiles. The smaller scale-length of the nebula related to the core-dominated RLQ would be consistent with the ionising emission from the QSO having an orientation closer to the sight line than for the RQQ.

Apart from jet interactions, other effects could determine the properties and correlations we find for the EELRs. Firstly, the quasar ionising luminosity could be the main factor determining the nebula luminosity. In this case it is expected that the continuum luminosity from RLQs should be brighter than

from RQQs, which is in contradiction with the predicted 912 Å luminosity. The statistical tests give no evidence for a correlation of the line emission with the quasar ionising luminosity. Secondly, the velocities inferred from the line widths of the Ly α lines from the EELRs around RLQs could suggest a disturbed medium relative to the EELRs around RQQs. In the H91b sample of RLQs the nebular Ly α line widths are 700–1000 km s $^{-1}$, which is slightly larger than the \sim 500 km s $^{-1}$ found in this IFS study. Radio galaxies show Ly α line fluxes similar to the bright objects in this sample and have velocity dispersions of about 1000 km s $^{-1}$ (van Ojik et al. 1997), while the quiescent component of the EELRs around radio-galaxies (Villar-Martín et al. 2003) have velocities similar to those studied here.

Alternatively, external conditions can be responsible for the flux differences. One can suspect that the RQQs reside in less dense environments (see e.g. van Ojik et al. 1997). The electron density n_e is proportional to the luminosity $L_{\text{Ly}\alpha}$ divided by the volume of the cloud V times the covering factor f (i.e. $n_e^2 \propto \frac{L_{\text{Ly}\alpha}}{fV}$, see Villar-Martín et al. 2003). Since we find that both the volume and the luminosity of the EELRs are smaller for RQQ, this would imply that the density is roughly the same (around 10–100 cm $^{-3}$ for $f = 10^{-5}$). As we argue the masses for the RQQ nebulae are smaller, this would imply that RQQ exist in less dense surroundings.

Nevertheless, observations of the host galaxies of the two populations at low redshifts ($z < 0.25$) indicate no differences for quasars with similar nuclear powers (Dunlop et al. 2003). At higher redshifts little is known about the environments of RQQs, but there is evidence that RLQs reside in higher density environments (e.g. Hall & Green 1998; Sánchez & González-Serrano 1999, 2002) compared to RQQs. Those studies focused on the stellar light whereas we look at emission line gas. Rich environments are expected to have more gas by nature, and by evolution. Captured galaxies suffer from a stripping effect due to harassment and tidal effects, and the gas is ejected from the galaxies into the intergalactic medium. Such differences in the environment could affect the Ly α emission we detect. We know that the Ly α flux detected is a strict lower limit because of resonance scattering and dust absorption. We find evidence for resonance scattering in the brightest emission lines that show red asymmetries. This effect may not affect the luminosity detected from the EELRs significantly. The general lack of Lyman limit breaks in QSO spectra places strong constraints on the amount of neutral gas present along the sight lines. This is in contrast to high redshift radio galaxies, where 60% of the galaxies show strong absorption lines that indicate the presence of large amounts of neutral gas (van Ojik et al. 1997).

Extended C IV and He II emission has been observed in one RLQ which also has extended Ly α emission (Lehnert & Becker 1998), but most RLQs only have upper limits for the C IV line flux (Heckman et al. 1991a). For the two brightest objects considered here, where the tightest constraints can be made, we find upper limits of the flux ratio $f(\text{C IV})/f(\text{Ly}\alpha) < 0.1$. The limit is comparable to the smallest values found for radio galaxies. A small value can be caused

by a difference in the viewing angle, or a low ionisation parameter (Villar-Martin et al. 1996). Another explanation is that the objects studied here have less metal enriched surroundings (see Weidinger et al. 2005), i.e. again suggesting that the environment is different.

Finally, we must consider the possibility that the EELRs around the RQQs are caused by infalling material which is ionised by the QSO. In fact, the properties of the EELRs are similar to the flux and extension calculated from theoretical predictions in the case of matter falling into dark matter halos (Haiman & Rees 2001). Assuming infalling matter with a certain density profile, Weidinger et al. (2005) modeled their observed surface brightness and velocity structure from a long slit spectrum of Q1205–30. The structure of that nebula is quite similar to the one-dimensional structure we extract for Q1425+606. The interpretation of the nebulae structure and fluxes in the infall scenario will depend strongly on the ambient density, and variations in the nearby environment could cause differences such as we find in the sample studied here.

6. Conclusions

Quasars are believed to reside in the most massive dark matter halos at the centers of galaxies, and by studying quasars we can trace the formation and evolution of massive galaxies at high redshifts. The growth of massive galaxies has been suggested to be regulated by feedback from quasars. On the other hand, the formation of massive galaxies require large amounts of gas to be present to form stars and falling in to feed the quasar itself. Hence the evolution of massive galaxies must be balanced between infall and feedback mechanisms, both equally important for galaxy formation.

To investigate the impact of quasars on the surrounding gas, we have observed extended emission from gas around very bright quasars at $z \approx 3$. We find indications for correlations between the luminosities and sizes of EELRs around RQQs and compare them to those already known for RLQs. The scaling relations could indicate that the interaction of the radio jets with the surrounding gas enhances the luminosity of the EELRs around RLQs. Since RQQ comprise about 90% of powerful AGN, the EELRs from RQQs seem more suitable to study the effects of the central QSOs on the surrounding gas. Surprisingly, the ionising fluxes at the Lyman limit for the QSOs themselves seem not to determine the properties for the EELRs, since no correlations are found, whereas there is a strong correlation between the EELR luminosities and the integrated broad line Ly α luminosity for the five QSOs investigated. Why there is this discrepancy has yet to be understood.

The sample studied here is very small, and correlations could be biased because of small number statistics. Future investigations must involve a well defined sample to examine RLQs and RQQs at similar redshifts using the same technique to study the interaction between the radio power, morphology and luminosities of the EELRs.

Acknowledgements. L. Christensen acknowledges support by the German Verbundforschung associated with the ULTROS project, grant no. 05AE2BAA/4. K. Jahnke acknowledges support from DLR

project no. 50 OR 0404. We thank the referee M. Villar-Martín for very thorough and detailed comments.

References

Antonucci, R. R. J., Kinney, A. L., & Ford, H. C. 1989, *ApJ*, 342, 64

Barthel, P. D. 1989, *ApJ*, 336, 606

Benn, C. R., Vigotti, M., Carballo, R., Gonzalez-Serrano, J. I., & Sánchez, S. F. 1998, *MNRAS*, 295, 451z

Bergeron, J., Petitjean, P., Cristiani, S., et al. 1999, *A&A*, 343, L40

Bremer, M. N., Fabian, A. C., Sargent, W. L. W., et al. 1992, *MNRAS*, 258, 23

Bunker, A., Smith, J., Spinrad, H., Stern, D., & Warren, S. 2003, *Ap&SS*, 284, 357

Christensen, L. 2005, PhD thesis, Potsdam University

Christensen, L., Jahnke, K., Wisotzki, L., et al. 2006, *A&A* accepted

Christensen, L., Sanchez, S. F., Jahnke, K., et al. 2004, *A&A*, 417, 487

Crawford, C. S. & Vanderriest, C. 2000, *MNRAS*, 315, 433

Croton, D. J., Springel, V., White, S. D. M., et al. 2006, *MNRAS*, 365, 11

Di Matteo, T., Springel, V., & Hernquist, L. 2005, *Nature*, 433, 604

Dunlop, J. S., McLure, R. J., Kukula, M. J., et al. 2003, *MNRAS*, 340, 1095

Durret, F., Pecontal, E., Petitjean, P., & Bergeron, J. 1994, *A&A*, 291, 392

Fried, J. W. 1998, *A&A*, 331, L73

Fynbo, J. U., Thomsen, B., & Møller, P. 2000, *A&A*, 353, 457

Haiman, Z. & Rees, M. J. 2001, *ApJ*, 556, 87

Hall, P. B. & Green, R. F. 1998, *ApJ*, 507, 558

Heckman, T. M., Lehnert, M. D., Miley, G. K., & van Breugel, W. 1991a, *ApJ*, 381, 373

Heckman, T. M., Miley, G. K., Lehnert, M. D., & van Breugel, W. 1991b, *ApJ*, 370, 78

Hook, I. M., McMahon, R. G., Irwin, M. J., & Hazard, C. 1996, *MNRAS*, 282, 1274

Hopkins, P. F., Strauss, M. A., Hall, P. B., et al. 2004, *AJ*, 128, 1112

Hu, E. M. & Cowie, L. L. 1987, *ApJ*, 317, L7

Hu, E. M., McMahon, R. G., & Egami, E. 1996, *ApJ*, 459, L53

Isobe, T., Feigelson, E. D., & Nelson, P. I. 1986, *ApJ*, 306, 490

Jahnke, K., Sánchez, S. F., Wisotzki, L., et al. 2004, *ApJ*, 614, 568

Koratkar, A. P., Kinney, A. L., & Bohlin, R. C. 1992, *ApJ*, 400, 435

Lehnert, M. D. & Becker, R. H. 1998, *A&A*, 332, 514

McCarthy, P. J., Spinrad, H., & van Breugel, W. 1995, *ApJS*, 99, 27

Møller, P., Warren, S. J., Fall, S. M., Jakobsen, P., & Fynbo, J. U. 2000, *The Messenger*, 99, 33

Petitjean, P., Pecontal, E., Valls-Gabaud, D., & Charlot, S. 1996, *Nature*, 380, 411

Roth, M. M., Bauer, S., Dionies, F., et al. 2000, in Proc. SPIE, Vol. 4008, 277–288

Roth, M. M., Kelz, A., Fechner, T., et al. 2005, *PASP*, 117, 620

Sánchez, S. F., García-Lorenzo, B., Mediavilla, E., González-Serrano, J. I., & Christensen, L. 2004, *ApJ*, 615, 156

Sánchez, S. F. 2004, *AN*, 325, 167

Sánchez, S. F., García-Lorenzo, B., Jahnke, K., et al. 2006, *New Astronomy Review*, 49, 501

Sánchez, S. F. & González-Serrano, J. I. 1999, *A&A*, 352, 383

Sánchez, S. F. & González-Serrano, J. I. 2002, *A&A*, 396, 773

Schlegel, D. J., Finkbeiner, D. P., & Davis, M. 1998, *ApJ*, 500, 525

Scott, J. E., Kriss, G. A., Brotherton, M., et al. 2004, *ApJ*, 615, 135

Songaila, A. 2004, *AJ*, 127, 2598

Springel, V., Di Matteo, T., & Hernquist, L. 2005, *ApJ*, 620, L79

Steidel, C. C., Dickinson, M., & Sargent, W. L. W. 1991, *AJ*, 101, 1187

Tytler, D. & Fan, X.-M. 1992, *ApJS*, 79, 1

van Ojik, R., Roettgering, H. J. A., Miley, G. K., & Hunstead, R. W. 1997, *A&A*, 317, 358

Vanden Berk, D. E., Richards, G. T., Bauer, A., et al. 2001, *AJ*, 122, 549

Villar-Martín, M., Binette, L., & Fosbury, R. A. E. 1996, *A&A*, 312, 751

Villar-Martín, M., Sánchez, S. F., De Breuck, C., et al. 2005, *MNRAS*, L112

Villar-Martín, M., Vernet, J., di Serego Alighieri, S., et al. 2003, *MNRAS*, 346, 273

Weidinger, M., Møller, P., & Fynbo, J. P. U. 2004, *Nature*, 430, 999

Weidinger, M., Møller, P., Fynbo, J. U., & Thomsen, B. 2005, *A&A*, 436, 825

White, S. D. M. & Frenk, C. S. 1991, *ApJ*, 379, 52

Wisotzki, L., Becker, T., Christensen, L., et al. 2003, *A&A*, 408, 455

List of Objects

- ‘Q0953+4749’ on page 3
- ‘PC 0953+4749’ on page 3
- ‘Q1347+112’ on page 3
- ‘Q1425+606’ on page 3
- ‘SBS 1425+606’ on page 3
- ‘Q1451+1223’ on page 3
- ‘B1451+123’ on page 3
- ‘Q1759+7539’ on page 3
- ‘GB2 1759+7539’ on page 3
- ‘Q1802+5616’ on page 3
- ‘PSS J1802+5616’ on page 3
- ‘Q2233+131’ on page 3